Stationary equilibrium torus supported by Weyssenhoff ideal spin fluid in Schwarzschild spacetime: Case of constant specific angular momentum distribution

Sayantani Lahiri[*] and Claus Lämmerzahl[†]

Center of Applied Space Technology and Microgravity (ZARM), 28359 Bremen, Germany

(Received 14 August 2023; accepted 27 November 2023; published 20 December 2023)

We consider a non-self-gravitating geometrically thick torus described by the Weyssenhoff ideal spin fluid in a black hole spacetime. The Weyssenhoff spin fluid shares the same symmetries of the background geometry, i.e., stationarity and axisymmetry and further describes circular orbital motion in the black hole spacetime. We further assume that the alignment of the spin is perpendicular to the equatorial plane. Under this setup, we determine the integrability conditions of the general relativistic momentum conservation equation of Weyssenhoff ideal spin fluid using the Frenkel spin supplementary condition. In light of the integrability conditions, we then present stationary equilibrium solutions of the spin fluid torus with constant specific angular momentum distributions around the Schwarzschild black hole by numerically solving the general relativistic momentum conservation equation. Our study reveals that both the isopressure and isodensity surfaces of torus get significantly modified in comparison to the ideal fluid torus without a spin fluid, owing to the spin tensor and its coupling to the curvature of the Schwarzschild black hole. In fact, the size of the torus is also found to be enhanced (diminished) depending on a positive (negative) magnitude of spin parameter s_0. We finally estimate the magnitude of s_0 by assuming the torus to be composed of spin-1/2 particles.

DOI: 10.1103/PhysRevD.108.123032

I. INTRODUCTION

The existence of black holes (BH) is one of the most profound theoretical predictions of general relativity (GR). Generally gravitational collapse of massive stars is thought to be responsible for the existence of BHs [1,2]. Today, it is widely believed that almost all galaxies in the observable universe possess supermassive BH at their center. This fact is supported by precision measurements, for example, in [3,4] in combination with the remarkable series of works [5–7]. Parallelly, significant support also comes out from the shadows of ultracompact central objects [8,9]. In recent times, an overwhelming support of this fact appeared from the images published by the Event Horizon Telescope Collaboration belonging to the shadow of the supermassive BH residing at the center of the M87 galaxy [10] and that of Sagittarius A* [11] at the center of the Milky Way. Furthermore, the observations of gravitational waves generated from the BH mergers provide evidence of BHs [12]. Additionally, there are also observational evidences for the existence of stellar-mass BHs through x-ray binaries, coming from the earliest observations [13,14], and more recently from electromagnetic observations [9,15–17] and gravitational wave observations [18].

The accretion of matter onto BHs or any compact object causes the conversion of enormous gravitational energy of the infalling accreting matter into its rotational energy (in the Newtonian case) and to radiation, part of which contributes to the luminous disklike structures [19] commonly known as an accretion disk (AD) surrounding the central compact object. Generally, ADs are found in diverse astrophysical scenarios, namely quasars, young stellar objects, cataclysmic variables, active galactic nuclei, microquasars, x-ray binaries, the central engine of short Gamma-ray bursts (GRBs), and kilonovae [20–26]. Depending on different features such as the optical depth, mass accretion rate, and geometrical thickness, they are categorized in different classes of models, namely geometrically thick disks or torus, thin disks, and advection-dominated accretion flows (see, for example, [27,28]).

The geometrical thick ADs, also known as Polish doughnuts, are the models which we will consider hereafter. These are stationary equilibrium configurations which can be constructed analytically. Typically modeled by a relativistic hydrodynamical fluid, the equilibrium configurations were initially constructed using the ideal fluid [29–33]. In recent years, different types of matter models have been considered for studying stationary equilibrium solutions, e.g., with a viscous fluid [34,35], with an electrically charged fluid [36–38], or by a magnetized fluid [39–41]. The studies concerning properties

[*]sayantani.lahiri@zarm.uni-bremen.de
[†]claus.laemmerzahl@zarm.uni-bremen.de

and morphologies of ADs located in different BH geometries have also been addressed in several works [42–47]. The studies with accretion in the presence of self-gravity effects can be found in many works [48–52].

It is worthwhile to note that previously different cosmological scenarios were studied by taking into consideration the Weyssenhoff fluid. For example, the status of the cosmological principle in the presence of Weyssenhoff fluid is investigated by Böhmer and Bronowski [53]. The consequences of Weyssenhoff fluid are investigated for addressing the dark energy of the universe [54], for averting initial cosmological singularity [53,55], and in describing the bouncing universe scenario [56]. However, to the best of our knowledge, the possible effects of spin fluid on stationary solutions of a torus have not been investigated so far. On that note, it is also likely that the constituents of a stationary torus may possess intrinsic spin angular momentum whose cumulative effects induce an overall nonzero spin of the fluid. Although spin is a microscopic property of matter, for the macroscopic description of matter, a corresponding hydrodynamical theory can be obtained by an averaging technique from the microscopic theory of matter with spin [57]. A prominent example is the phenomenological Weyssenhoff fluid model which describes classical ideal hydrodynamical fluid with spin [58] where the fluid elements are characterized by an intrinsic angular momentum, i.e., *spin* proportional to the volume. In this model, the spin angular momentum density is described by a second-rank antisymmetric tensor $S^{\mu\nu}$ whose spatial component is a three-vector that coincides with three-density of the spinning matter in the rest frame. Motivated by the attempt to look for experiments/observations for torsion, the Lagrangian formulation of the Weyssenhoff spin fluid model has been developed in the context of the Einstein-Cartan theory by taking torsion into consideration [59]. Moreover, using the Lagrangian formulation, it has been shown by Obukhov and Piskareva [60] that in general relativity, under the pole-dipole approximation, the conservation laws of the Weyssenhoff ideal spin fluid follows the generalized version of the evolution equation of spinning *test* particles given by Mathisson [61], Papapetrou [62], and Dixon [63], commonly known as Mathisson-Papapetrou-Dixon (MPD) equations. Additionally, in order to close the MPD equations a spin supplementary condition (SSC) has to be stated. The SSC is not unique. Several SSCs have been prescribed in the literature [64–69]. Notably, the conservation laws of the Weyssenhoff ideal spin fluid are obtained by adopting the Frenkel SSC [59,60]. Analogous to test particles with spin, the spin of the Weyssenhoff fluid interacts with the curvature of the background geometry leading to an additional spin-curvature coupling contribution in the momentum balance. Following this, a torus endowed with Weyssenhoff spin fluid thus allows us to examine the direct influences of spacetime curvature effects of the central compact object through the spin-curvature coupling term on the stationary solutions of the torus.

In the present work, we examine the consequences of spin-curvature coupling on stationary equilibrium solutions of relativistic torus modeled by the Weyssenhoff ideal spin fluid. We have adopted the test-fluid approximation, and thus, neglected any self-gravity effects of the torus. We start with a stationary and axisymmetric BH background where the spin fluid describes circular orbits and is endowed with constant specific orbital angular momentum distribution. In this background geometry, the integrability conditions of the general relativistic momentum conservation equation of ideal Weyssenhoff spin fluid are derived by considering the spin being aligned perpendicular to the equatorial plane. Our study reveals the newly obtained integrability conditions of the spin fluid embody the integrability conditions of the ideal fluid without spin, i.e., relativistic Von-Zeipel conditions. Additional conditions are obtained due to the presence of a spin tensor and its coupling to the spacetime curvature of the stationary, axisymmetric BH geometry.

In order to determine the impacts of spin and curvature on stationary solutions of a torus, we consider the simplest nonrotating background geometry, i.e., a Schwarzschild BH. Using the integrability condition, we then present the allowed structure of the spin tensor necessary to produce macroscopic spin effects on the morphology of the torus. Here, we consider the scenario when the fluid within the torus exactly fills its Roche lobe. Under this situation, the equilibrium stationary solutions of the torus are constructed by semianalytically solving the general relativistic momentum conservation equation of Weyssenhoff fluid with constant specific angular momentum distributions. The corresponding solutions are then used to construct the isopressure and the isodensity surfaces of the torus. By comparing with a torus described with only ideal fluid without spin, our analysis reveals that the spin tensor-curvature coupling plays a crucial role in modifying the overall morphology of the torus as well as altering the locations of its cusp, center, and outer edge. The qualitative effects of the spin on the torus is characterized by a parameter s_0, and the size and total energy density of the torus are found to be either enhanced or reduced depending on the magnitude and sign of s_0. In the simplest scenario, we have provided an estimation of s_0 by assuming that the torus is built with spin-$1/2$ particles.

The present paper is organized as follows. Section II begins with the mathematical framework of the Weyssenhoff ideal spin fluid model. Following this, the integrability conditions of the general relativistic momentum conservation equation of the Weyssenhoff spin fluid are presented. In Sec. III, we determine the complete structure of the spin tensor of the Weyssenhoff spin fluid which undergoes circular motion in the Schwarzschild spacetime. Using this, the stationary solutions of the equilibrium torus are constructed in the Schwarzschild

BH spacetime. We discuss the results pertaining to the effects of spin and curvature on the morphology of the torus by studying the isodensity and isopressure surfaces constructed from the stationary solutions in Sec. IV. Finally, after giving an estimation for s_0, in Sec. V, a summary of our study is presented.

A. Notations and conventions

We take Riemannian geometry with the signature $-,+,+,+$. The covariant derivative is denoted by ∇_μ. We will use geometrized units ($G = c = 1$) throughout the paper. The Greek indices represent the coordinate basis which runs from t, r, θ, ϕ.

II. PHYSICAL FRAMEWORK

A. The matter model

The aim of our work is to construct equilibrium solutions of a stationary torus composed of a fluid made of neutral particles with spin which can be of classical or quantum origin. In the continuum limit such a kind of matter can be described by the Weyssenhoff ideal neutral spin fluid [58]. In GR, the symmetric energy momentum tensor of the Weyssenhoff spin fluid model is given by [60]

$$T_{\mu\nu} = (\epsilon + p)u_\mu u_\nu + p g_{\mu\nu} + 2(g^{\rho\sigma} - u^\rho u^\sigma)\nabla_\rho[u_{(\mu}S_{\nu)\sigma}], \quad (1)$$

where ϵ and p are the energy density and pressure of the fluid. The round brackets in (1) denote the symmetrization of μ and ν indices. The four-velocity u^μ of the spinning fluid constituents is normalized as $u^\mu u_\mu = -1$. The projection tensor to the particle's rest frame is given by $\Delta^{\mu\nu} = g^{\mu\nu} + u^\mu u^\nu$. Finally, $S^{\mu\nu}$ is the antisymmetric spin tensor that corresponds to the dipole contribution in the context of multipole moment expansion [58]. The Weyssenhoff spin fluid model employs the Frenkel SSC, alternatively known as the Mathisson-Pirani SSC, given by

$$S^{\mu\nu}u_\nu = 0. \quad (2)$$

This defines u^μ as the four-velocity of the center of mass of the spinning body.

The divergence of (1) and using the SSC (2) gives the momentum balance

$$(\epsilon + p)a_\mu + \partial_\mu p + 2\nabla_\rho(u^\rho S_{\mu\sigma}a^\sigma) + R_{\rho\sigma\tau\mu}S^{\rho\sigma}u^\tau = 0, \quad (3)$$

where the Riemann curvature tensor is defined as

$$R^\mu{}_{\nu\rho\delta} = \partial_\rho\Gamma^\mu_{\delta\nu} - \partial_\delta\Gamma^\mu_{\rho\nu} + \Gamma^\lambda_{\delta\nu}\Gamma^\mu_{\rho\lambda} - \Gamma^\lambda_{\rho\nu}\Gamma^\mu_{\delta\lambda} \quad (4)$$

and $\Gamma^\mu_{\rho\sigma}$ are the Christoffel symbols. The energy balance equation reads as follows:

$$D\epsilon + (\epsilon + p)\nabla_\mu u^\mu = 0, \quad (5)$$

where $D = u^\nu\nabla_\nu$ and the four-acceleration is given by $a^\mu = u^\nu\nabla_\nu u^\mu$. Equation (3) represents the MPD equation in our spin fluid model. We note that in the absence of spin (3) reduces to the Euler equation.

The spin four-vector is defined as

$$S_\mu = -\frac{1}{2}\epsilon_{\mu\nu\rho\sigma}u^\nu S^{\rho\sigma}, \quad (6)$$

and the inverse relation is given by

$$S^{\mu\nu} = -\epsilon^{\mu\nu\rho\sigma}S_\rho u_\sigma. \quad (7)$$

The spin density scalar is defined by

$$S^2 = \frac{1}{2}S_{\mu\nu}S^{\mu\nu}. \quad (8)$$

S depends on r and θ but is constant along each particle trajectory. Let us define the following quantity:

$$S^\mu{}_{\rho\sigma} = u^\mu S_{\rho\sigma}, \quad (9)$$

and by taking the divergence, one obtains

$$\begin{aligned}\nabla_\mu(u^\mu S^{\rho\sigma}) &= u^\rho u_\lambda\nabla_\mu(u^\mu S^{\lambda\sigma}) - u^\sigma u_\lambda\nabla_\mu(u^\mu S^{\lambda\rho}) \\ &= (u^\sigma S^{\lambda\rho} - u^\rho S^{\lambda\sigma})a_\lambda, \end{aligned} \quad (10)$$

which implies the divergence of $S^\mu{}_{\rho\sigma}$ is vanishing if the four-acceleration also vanishes or is orthogonal to the spin tensor.

B. Symmetries

In order to find solutions of the Weyssenhoff ideal spin fluid equation of motion we need to assume the following symmetry conditions:

(i) The BH background spacetime is stationary and axisymmetric. The corresponding Killing vectors are given by $\eta^\mu = \partial_t = (1, 0, 0, 0)$ and $\xi^\mu = \partial_\phi = (0, 0, 0, 1)$. Accordingly, the Lie derivatives along ξ and η of all geometric quantities vanish.

(ii) The Weyssenhoff spin fluid shares the same symmetries of the background geometry; therefore, any (tensorial) flow parameter f, including the spin, satisfies the conditions $\mathcal{L}_\eta f = 0$ and $\mathcal{L}_\xi f = 0$, where $\mathcal{L}$ is the Lie derivative. Accordingly, in an adapted coordinate system all quantities depend on r and θ only. This represents a major restriction. However, our aim is to determine the order of magnitude the spin induced changes of the shape of ADs for which special situations are fine.

(iii) The spin fluid describes circular orbits, and therefore the four-velocity of the fluid is given by

$$u^\mu = (u^t, 0, 0, u^\phi). \quad (11)$$

This fluid does not constitute a stationary congruence. The angular velocity then is

$$\Omega = \frac{d\phi}{dt} = \frac{u^\phi}{u^t}, \tag{12}$$

and the specific orbital angular momentum is

$$-l = \frac{p_\phi}{p_t} = \frac{g_{\phi\mu}u^\mu}{g_{t\nu}u^\nu} = \frac{g_{\phi t}u^t + g_{\phi\phi}u^\phi}{g_{tt}u^t + g_{t\phi}u^\phi}. \tag{13}$$

We have

$$l = -\frac{g_{\phi t} + g_{\phi\phi}\Omega}{g_{tt} + g_{t\phi}\Omega}, \qquad \Omega = -\frac{g_{t\phi} + g_{tt}l}{g_{\phi\phi} + g_{t\phi}l}. \tag{14}$$

The four-velocity can be written as

$$u^\mu = A(\eta^\mu + \Omega\xi^\mu) \tag{15}$$

with

$$A = u^t = \frac{1}{\sqrt{g_{tt} + 2g_{t\phi}\Omega + g_{\phi\phi}\Omega^2}}, \tag{16}$$

$$-u_t = \sqrt{\frac{g_{t\phi}^2 - g_{tt}g_{\phi\phi}}{l^2 g_{tt} + 2l g_{t\phi} + g_{\phi\phi}}}. \tag{17}$$

The four-acceleration then can be computed as

$$a_\mu = \partial_\mu \ln u_t - \frac{\Omega\partial_\mu l}{(1-\Omega l)} = \partial_\mu \ln u^t - \frac{l\partial_\mu\Omega}{1-\Omega l}. \tag{18}$$

Such smooth orbital conditions are not compatible with all SSCs [69].

(iv) The spin four-vector S^ν is aligned perpendicular to the equatorial plane; i.e., the spin vector is polar and is given by

$$S^\nu = S^\theta \delta^\nu_\theta. \tag{19}$$

Then the nonzero components of the spin tensor can be calculated from (7)

$$S^{tr} = -S\sqrt{\frac{g_{\theta\theta}}{-g}}u_\phi, \tag{20}$$

$$S^{r\phi} = -S\sqrt{\frac{g_{\theta\theta}}{-g}}u_t, \tag{21}$$

where S is the spin scalar density (8) and is given by $S = \sqrt{g_{\theta\theta}}S^\theta$.

C. Integrability conditions

In this section, we will determine the existence of integrability conditions of (3). Using Eq. (10), one obtains

$$\begin{aligned}\nabla_\rho(u^\rho S_{\mu\sigma}a^\sigma) &= g_{\mu\alpha}g_{\sigma\beta}\nabla_\rho(u^\rho S^{\alpha\beta}a^\sigma)\\ &= g_{\mu\alpha}g_{\sigma\beta}[\nabla_\rho(u^\rho S^{\alpha\beta})a^\sigma + u^\rho S^{\alpha\beta}(\nabla_\rho a^\sigma)]\\ &= g_{\mu\alpha}g_{\sigma\beta}[(u^\beta S^{\lambda\alpha} - u^\alpha S^{\lambda\beta})a_\lambda] + S_{\mu\sigma}Da^\sigma\\ &= S^\lambda_\mu a_\lambda(u_\sigma a^\sigma) - S^{\lambda\beta}a_\lambda a_\beta u_\mu + S_{\mu\sigma}Da^\sigma\\ &= S_{\mu\beta}Da^\beta,\end{aligned} \tag{22}$$

where $u_\sigma a^\sigma = 0$ and $S^{\lambda\beta}a_\lambda a_\beta = 0$. Hence (3) reduces to

$$(\epsilon + p)a_\mu + \partial_\mu p + 2S_{\mu\beta}Da^\beta + R_{\rho\sigma\tau\mu}S^{\rho\sigma}u^\tau = 0. \tag{23}$$

Note that (23) further reduces to the Euler equation in the absence of the spin. Since the fluid undergoes circular motion, the rate of the change in acceleration can be considered to be proportional to the four-acceleration. This implies that one can make the following ansatz for the term Da^β in (3):

$$Da^\beta = \Omega^{\beta\nu}a_\nu, \tag{24}$$

where $\Omega_{\alpha\beta}$ is the antisymmetric angular velocity tensor satisfying $\Omega_{\alpha\beta} = -\Omega_{\beta\alpha}$. Using (15), the last term in (3) can be written as

$$R_{\rho\sigma\tau\mu}S^{\rho\sigma}u^\mu = A(R_{\rho\sigma\tau\mu}S^{\rho\sigma}\eta^\mu + \Omega R_{\rho\sigma\tau\mu}S^{\rho\sigma}\xi^\mu). \tag{25}$$

Let us make an ansatz and express it as follows:

$$R_{\alpha\beta\gamma\mu}S^{\alpha\beta}\eta^\gamma = \partial_\mu\Phi, \tag{26}$$

$$R_{\alpha\beta\gamma\mu}S^{\alpha\beta}\xi^\gamma = \partial_\mu\phi, \tag{27}$$

where the scalars ϕ and Φ are functions of r and θ. Note that $\mathcal{L}_\eta(R_{\alpha\beta\gamma\mu}S^{\alpha\beta}) = \mathcal{L}_\xi(R_{\alpha\beta\gamma\mu}S^{\alpha\beta}) = 0$ since due to the symmetries, the Lie derivatives of the Riemann curvature tensor and spin tensor along the Killing vectors η and ξ vanish. Substituting (24), (26), (27), and (18) into (23) we obtain

$$\begin{aligned}\frac{\partial_\mu p}{\epsilon + p} = &-\partial_\mu \ln(-u_t) + \frac{\Omega\partial_\mu l}{1-\Omega l}\\ &- \frac{2S_{\mu\alpha}\Omega^{\alpha\beta}a_\beta}{\epsilon + p} - \frac{A(\partial_\mu\Phi + \Omega\partial_\mu\phi)}{\epsilon + p}\end{aligned} \tag{28}$$

or, equivalently,

$$\begin{aligned}\frac{\partial_\mu p}{\epsilon + p} = &-\partial_\mu \ln(-u^t) + \frac{l\partial_\mu\Omega}{1-\Omega l}\\ &- \frac{S_{\mu\alpha}\Omega^{\alpha\beta}a_\beta}{\epsilon + p} - \frac{A(\partial_\mu\Phi + \Omega\partial_\mu\phi)}{\epsilon + p}.\end{aligned} \tag{29}$$

The integrability condition then reads

$$0 = \frac{\partial_{[\mu} p \partial_{\nu]} \epsilon}{(\epsilon+p)^2} - \frac{\partial_{[\mu} l \partial_{\nu]} \Omega}{(1-\Omega l)^2} - \partial_{[\mu}\Phi\partial_{\nu]}\left(\frac{A}{\epsilon+p}\right) + \partial_{[\mu}\phi\partial_{\nu]}\left(\frac{\Omega A}{\epsilon+p}\right) - \partial_\mu\left(\frac{2S_{\nu\alpha}\Omega^{\alpha\beta}a_\beta}{\epsilon+p}\right) + \partial_\nu\left(\frac{2S_{\mu\alpha}\Omega^{\alpha\beta}a_\beta}{\epsilon+p}\right), \tag{30}$$

where the square brackets denote antisymmetrization. Here all terms are independent from the others: the first term is on energy and pressure, the second on angular velocity and momentum, and the last two are on spin coupling. Accordingly, we require that each term should vanish separately. The first term vanishes provided $\partial_\mu\epsilon \sim \partial_\mu p$, the second term vanishes for $\partial_\mu\Omega \sim \partial_\mu l$, and for the other two terms we require $\partial_\mu\Phi \sim \partial_\mu \frac{A}{\epsilon+p}$ and $\partial_\mu\phi \sim \partial_\mu \frac{\Omega A}{\epsilon+p}$. Since the last two terms of Eq. (30) must also vanish, this then means,

$$\epsilon = \epsilon(p), \tag{31}$$

$$\Omega = \Omega(l), \tag{32}$$

$$\Phi = \Phi\left(\frac{A}{\epsilon+p}\right), \tag{33}$$

$$\phi = \phi\left(\frac{\Omega A}{\epsilon+p}\right), \tag{34}$$

$$\partial_\mu B = \frac{2S_{\mu\alpha}\Omega^{\alpha\beta}a_\beta}{\epsilon+p}; \tag{35}$$

that is, we obtain a number of equations of states between ϵ and p (barotropic equation of state), between Ω and l, between Φ and $\frac{A}{\epsilon+p}$, and between ϕ and between $\frac{\Omega A}{\epsilon+p}$. The integrability condition of an ideal fluid in the absence of spin is only given by (31).[1] In the stationary and axisymmetric spacetime, where the spin of the fluid undergoing circular motion is aligned along a specific orientation [see (19)], one readily concludes that the function B is independent of the coordinates t and ϕ. Therefore, from (35), one obtains for $\mu = t$ and $\mu = \phi$ the following conditions:

$$\partial_t B = S_{tr}\Omega^{rr}a_r + S_{tr}\Omega^{r\theta}a_\theta = 0, \tag{36}$$

$$\partial_\phi B = S_{\phi r}\Omega^{rr}a_r + S_{\phi r}\Omega^{\phi\theta}a_\theta = 0. \tag{37}$$

[1]The integrability condition of the Euler equation in the absence of spin is commonly known as the Von-Zeipel condition [30].

Given the fact that $\Omega^{rr} = 0$, it follows that $\Omega^{r\theta} = 0$ from the above conditions. Also $\partial_\theta B = S_{\theta\alpha}\Omega^{\alpha r}a_r + S_{\theta\alpha}\Omega^{\alpha\theta}a_\theta = 0$ as $S_{\theta\alpha} = 0$ due to (19). Therefore the integrability condition holds provided $B = B(r)$ and is determined from (35) using (20) and (21). Hence (23) is expressed in the integral form as

$$\ln|u_t| - \int_0^l \frac{\Omega dl}{1-\Omega l} + \int_0^p \frac{dp}{\epsilon+p} + \int dB + \int_0^\Phi \frac{A(r,\theta)d\Phi}{\epsilon+p} + \int_0^\phi \frac{\Omega A(r,\theta)d\phi}{\epsilon+p} = \text{const.} \tag{38}$$

At the surface and on the inner edge of the disk, both the pressure and the energy density of the fluid vanish. Also at the radial position of the inner edge, i.e., $r = r_{\rm in}$, one can usually express $l = l_{\rm in}$, $u_t = u_{t_{\rm in}}$, and $\Phi_{\rm in} = 0 = \phi_{\rm in}$. Therefore Eq. (38) becomes

$$W - W_{\rm in} + \int_0^p \frac{dp}{\epsilon+p} + \int_0^{r_{\rm in}} dB + \int_0^\Phi \frac{A(r,\theta)d\Phi}{\epsilon+p} + \int_0^\phi \frac{\Omega A(r,\theta)d\phi}{\epsilon+p} = 0. \tag{39}$$

The total potential is given by

$$W - W_{\rm in} = \ln|u_t| - \ln|u_{t_{\rm in}}| - \int_{l_{\rm in}}^l \frac{\Omega dl}{1-\Omega l}, \tag{40}$$

and $W_{\rm in}$ is the total potential at the inner edge of the torus at the equatorial plane.

III. EQUILIBRIUM TORI WITH WEYSSENHOFF SPIN FLUID

A. Methodology

Let us now consider a relativistic non-self-gravitating torus described by the Weyssenhoff ideal spin fluid in static, nonrotating BH spacetime, described by the Schwarzschild metric. In a simplified setup, the torus is characterized by constant specific orbital angular momentum distribution. The spin fluid in the torus is in hydrostatic equilibrium, shares the same symmetries of the Schwarzschild BH [see (19)–(21)], and undergoes purely circular orbits. In addition, we assume the internal energy density, ε, is very small, and, therefore, the total energy is approximately equal to the rest-mass density, i.e., $\epsilon = \rho(1+\varepsilon) \approx \rho$. In Schwarzschild coordinates, the Schwarzschild metric is given by

$$ds^2 = g_{tt}dt^2 + g_{rr}dr^2 + g_{\theta\theta}d\theta^2 + g_{\phi\phi}d\phi^2, \tag{41}$$

where $0 < t < \infty$, $0 \le r \le \infty$, $0 \le \theta \le \pi$, and $0 \le \phi \le 2\pi$. The metric coefficients are

$$g_{tt} = -\left(1 - \frac{2M}{r}\right) = -\frac{1}{g_{rr}}, \quad g_{\theta\theta} = r^2, \quad g_{\phi\phi} = r^2\sin^2\theta, \tag{42}$$

where M is the mass parameter of the Schwarzschild BH which is set as $M = 1$ in the rest of the paper. As $g_{t\phi} = 0$ for a nonrotating spacetime, the specific angular momentum and the angular velocity are related as

$$\frac{l(r,\theta)}{\Omega(r,\theta)} = -\frac{g_{\phi\phi}}{g_{tt}}. \tag{43}$$

With the assumption of constant specific angular momentum distributions, we set $l(r,\theta) = l_0$ where l_0 is a constant and is in accordance to the integrability condition [see (31)], and we consider the equation of state as $p = \kappa\epsilon^\gamma$, so that (23) is expressed as

$$\partial_\mu \epsilon = \frac{(\epsilon^{2-\gamma} + \kappa\epsilon)}{-\kappa\gamma}\partial_\mu \ln(-u_t) - \frac{(2S_{\alpha\beta}Da^\beta + R_{\rho\sigma\tau\mu}S^{\rho\sigma}u^\tau)}{\kappa\gamma\epsilon^{\gamma-1}}, \tag{44}$$

where κ is the polytropic constant and γ is the adiabatic coefficient. Using (20) and (21), radial and polar components of (44) can be read off as follows:

$$\partial_r \epsilon = \frac{(\epsilon^{2-\gamma} + \kappa\epsilon)}{-\kappa\gamma}\partial_r \ln(-u_t) - \frac{S(r,\theta)}{\kappa\gamma\epsilon^{\gamma-1}(1-\Omega l_0)}\sqrt{\frac{g_{\theta\theta}}{-g}}F_1 - \frac{2g_{rr}g_{tt}S(r,\theta)}{\kappa\gamma\epsilon^{\gamma-1}}\sqrt{\frac{g_{\theta\theta}}{-g}}\left[u_\phi Da^t - \frac{g_{\phi\phi}}{g_{tt}}u_t Da^\phi\right], \tag{45}$$

$$\partial_\theta \epsilon = \frac{(\epsilon^{2-\gamma} + \kappa\epsilon)}{-\kappa\gamma}\partial_\theta \ln(-u_t) - \frac{S(r,\theta)}{\kappa\gamma\epsilon^{\gamma-1}(1-\Omega l_0)}\sqrt{\frac{g_{\theta\theta}}{-g}}F_2, \tag{46}$$

where F_1 and F_2 are given by

$$F_1(r,\theta) = -\Omega l_0 R_{tr\phi r} + \Omega R_{r\phi\phi r} - l_0 R_{trtr} + R_{r\phi tr},$$
$$F_2(r,\theta) = -\Omega l_0 R_{tr\phi\theta} + \Omega R_{r\phi\phi\theta} - l_0 R_{trt\theta} + R_{r\phi t\theta}.$$

To obtain F_1 and F_2 the following relations are used:

$$u_\phi u^t = \frac{l}{1-\Omega l_0}, \qquad u_t u^\phi = -\frac{\Omega}{1-\Omega l_0}. \tag{47}$$

The nonzero components of the curvature tensor appearing in $F_1(r,\theta)$ and $F_2(r,\theta)$ are

$$R_{trtr} = -\frac{2}{r^3}, \qquad R_{r\phi\phi r} = \frac{\sin^2\theta}{(r-2)}, \tag{48}$$

so that $F_1(r,\theta)$ and $F_2(r,\theta)$ finally reduce to

$$F_1(r,\theta) = \frac{3l_0}{r^3}, \qquad F_2(r,\theta) = 0. \tag{49}$$

The stationary solutions of the equilibrium ideal spin fluid torus are then obtained by computing the energy density and the pressure which are determined by solving (45) and (46) for a spin length function S along with the values of the constants κ and γ.

The existence of integrability conditions imply $dp/(\epsilon + p)$ is an exact differential [see (38)], and as a result, the compatibility condition $\partial_\theta\partial_r p = \partial_r\partial_\theta p$ expressed as the commutation of partial second derivatives of the fluid pressure is automatically satisfied. We utilize the compatibility condition for determining the spin length function as discussed in the following section.

B. Determination of spin length function

In order to obtain the solutions of fluid pressure and energy density, we must assign values for κ, γ, and determine the spin length function S. In view of the fact that the Weyssenhoff fluid shares the same symmetries as that of the background geometry, S is therefore purely a function of radial and polar coordinates. The value of the adiabatic index is chosen to be $\gamma = 2$. The fluid pressure and the energy density are then related by the equation of state as $p = \kappa\epsilon^2$. Note that this choice is high for any physical systems, but taking this value of the adiabatic index makes it convenient to perform analytic integration for our simple model of spin fluid torus presented here. We start with a general form of S as

$$S(r,\theta) = s_0 k(r,\theta)\epsilon^{\gamma-1}(1-\Omega l_0). \tag{50}$$

Here s_0 is a constant that can take both positive and negative values.

Substituting $\gamma = 2$ in (50), (45), and (46), one immediately obtains

$$\partial_r \epsilon = -\frac{(1+\kappa\epsilon)}{2\kappa}\partial_r \ln(-u_t) - \frac{l_0 s_0 k \csc\theta[l_0^2(r-2)^2\csc^2\theta(3-r\csc^2\theta)+(r-3)r^3]}{\kappa(r-2)r^4(r^3-l_0^2(r-2)\csc^2\theta)}, \tag{51}$$

$$\partial_\theta \epsilon = -\frac{(1+\kappa\epsilon)}{2\kappa}\partial_\theta \ln(-u_t). \tag{52}$$

Note that (51) and (52) reduce to the Euler equation valid for an ideal fluid for $s_0 = 0$. With our choice of the equation of state, the compatibility condition on the fluid pressure also implies second derivatives of energy density commute as $\partial_\theta\partial_r\epsilon = \partial_r\partial_\theta\epsilon$. Substituting (51) and (52) in the compatibility condition, the first order differential equation for $k(r,\theta)$ can be read off as

$$\partial_\theta k + \frac{P_1(r,\theta)}{P_2(r,\theta)}k = 0, \tag{53}$$

where

$$\frac{P_1(r,\theta)}{P_2(r,\theta)}=\frac{\cot\theta[l_0^2(r-2)\{(r-2)\csc^2\theta(20r^4-10l_0^2(r-2)r\csc^2\theta+3l_0^2(r-2))+3r^3(24-11r)\}+2r^6\sin^2\theta(12-5r)]}{2l_0^2(r-2)[(r-2)\csc^2\theta(2l_0^2(r-2)r\csc^2\theta-3l_0^2(r-2)-2r^4)-2r^3(r-3)]-2r^6\sin^2\theta(12-5r)}.$$

The solution of $k(r,\theta)$ is obtained as follows by solving (53) analytically:

$$k(r,\theta)=\frac{2^{1/4}\sin^{5/2}\theta[l_0^2(r-2)-r^3\sin^2\theta]^{5/4}C_1(r)}{4l_0^2(r-2)^2(2r-3\sin^2\theta)+4(12-5r)r^3\sin^4\theta}, \tag{54}$$

where $C_1(r)$ is a constant of integration over θ and is fixed at the equatorial plane. Following (54), $C_1(r)$ at the equatorial plane can be readily expressed in terms of $k(r,\pi/2)$ and l_0 in the following way:

$$C_1(r)=k\left(r,\frac{\pi}{2}\right)\frac{4l_0^2(r-2)^2(2r-3)+4(12-5r)r^3}{2^{1/4}[l_0^2(r-2)-r^3]^{5/4}}. \tag{55}$$

For convenience and simplicity of the computations, we choose $k(r,\pi/2)=1$ which is the simplest possible choice at par with the integrability conditions. Using (54) and (50), the spin length function in terms of the energy density, s_0, and l_0 is finally given by

$$S(r,\theta)=s_0\frac{\sin^{5/2}\theta[l_0^2(r-2)^2(2r-3)+r^3(12-5r)]}{[l_0^2(r-2)^2(2r-3\sin^2\theta)+r^3(12-5r)\sin^4\theta]}\left[\frac{l_0^2(r-2)-r^3\sin^2\theta}{l_0^2(r-2)-r^3}\right]^{5/4}\epsilon(r,\theta)(1-\Omega l_0). \tag{56}$$

With the determination of the solutions of $\epsilon(r,\theta)$, the spin length function can easily be computed using (56) for the values of s_0 and l_0.

C. Results

We now obtain the stationary solutions of the energy density and pressure of the equilibrium torus modeled by the Weyssenhoff ideal spin fluid. By integrating Eq. (52) directly, the expression for the energy density is found to be

$$\epsilon(r,\theta)=\frac{2^{1/4}\kappa C_2(r)(r^3\sin^2\theta-l_0^2(r-2))^{1/4}-\sqrt{\sin\theta}}{\kappa\sqrt{\sin\theta}}, \tag{57}$$

and $C_2(r)$ is the radial coordinate dependent constant of integration independent of θ. It is determined from the first order ordinary differential equation at the equatorial plane [about which the spin is defined by (19)] by substituting (57) in (51) as follows:

$$\frac{dC_2}{dr}+\frac{(3r-4)}{4r(r-2)}C_2 -\frac{l_0 s_0[l_0^2(r-2)^2(2r-3)+r^3(12-5r)]}{2\kappa.2^{1/4}(r-2)r^4[r^3-l_0^2(r-2)]^{5/4}}=0. \tag{58}$$

The above equation is solved numerically under appropriate boundary conditions which when substituted in (57) generates the isodensity and isopressure surfaces of the torus. We next describe the scheme for obtaining $C_2(r)$.

To demonstrate the effects of spin fluid on the equilibrium structure of a torus, we mainly concentrate on a closed torus configuration which is characterized by its cusp $r_{\rm cusp}$ that corresponds to the radial location where the isopressure and isodensity surfaces self-cross, center $r_{\rm c}$ that corresponds to the location of maximum pressure and energy density, the inner edge $r_{\rm in}$, and an outer edge $r_{\rm out}$, all defined at the equatorial plane. Furthermore, we build stationary models of equilibrium torus for which the fluid exactly fills the Roche lobe. In terms of the effective potential, this amounts to the potential gap $\triangle W$ reducing to $\Delta W=W_{\rm in}-W_{\rm cusp}=0$ where $W_{\rm in}$ and $W_{\rm cusp}$ are the respective effective potentials of the inner edge and the cusp at the equatorial plane [70]. Consequently, the inner edge of the torus coincides with the cusp at the equatorial plane.

Since for an exactly filling torus configuration with $\triangle W=0$ corresponds to $p(r_{\rm in})=\epsilon(r_{\rm in})=0$ at $r_{\rm in}=r_{\rm cusp}$, using the condition $\epsilon(r_{\rm in})=0$ one then obtains the boundary condition for solving the differential equation for (58) as follows:

$$C_2(r_{\rm in})=\frac{1}{2^{1/4}\kappa(r_{\rm in}^3-l_0^2(r_{\rm in}-2))^{1/4}}. \tag{59}$$

The inner edge of the torus must be known to compute $C_2(r_{\rm in})$ which serves as the boundary condition for numerically solving (58) for given values of l_0 and s_0. Note that the cusp of the torus corresponds to the location of the extrema where isopressure and isodensity surfaces self-cross. In the

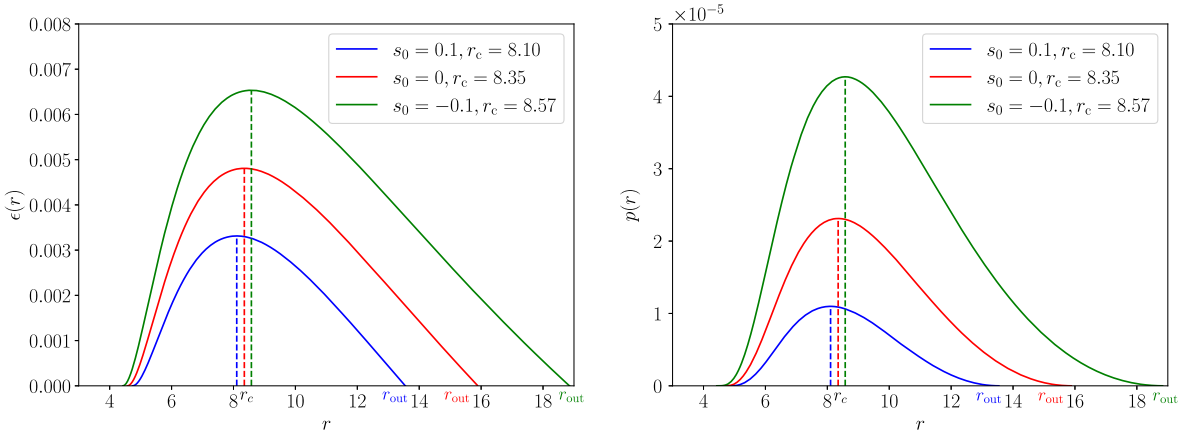

FIG. 1. Isodensity and isopressure profiles of Weyssenhoff spin torus at the equatorial plane for $s_0 > 0$, $s_0 = 0$, and $s_0 < 0$ with $l_0 = 3.8$. The red dotted line is the radial location of the center r_c of a torus without spin fluid ($s_0 = 0$). The shift in the radial position of r_c occurs by changing the magnitude of s_0 as shown by the blue dotted line for $s_0 = 0.1$ and the green dotted line for $s_0 = -0.1$. For each s_0, the outer edge of the torus r_{out} is shown.

present context, it coincides with the inner edge, therefore imposing the condition $\partial_r \epsilon(r = r_{in}) = 0$ in (51), together with (57) and (59), and the polynomial equation for determining the inner edge of the torus is found to be

$$r_{in}^6 - l_0^2(r_{in} - 2)^2 r_{in}^3 - l_0^3(r_{in} - 2)^2(2r_{in} - 3)s_0 + l_0 s_0(5r_{in} - 12)r_{in}^3 = 0, \quad (60)$$

where we have further set $\kappa = 1$. Out of all six possible roots of (60), the real positive root of $r_{in} > r_{Sch}$ is chosen, where r_{Sch} corresponds to the Schwarzschild radius.

On a different note, it can easily be observed that for $s_0 = 0$, one retrieves the Keplarian distribution given by $l_0 = \frac{r\sqrt{r}}{r-2} = l_k$, where l_k is the Keplarian specific angular momentum at r_{in} coinciding with r_{cusp} [31].

The isodensity surfaces of the equilibrium torus are constructed with two constant values of specific angular momentum, namely $l_0 = 3.8$ and $l_0 = 4$. We first consider $l_0 = 3.8$; for this value of l_0, solutions of closed equilibrium tori are obtained characterized by cusp, center, and a well-defined outer edge. The constant energy density profiles of such closed torus at the equatorial plane are shown in Fig. 1(a) for $s_0 = 0$, $s_0 = 0.1$, and $s_0 = -0.1$. Let us now discuss the procedure for obtaining the solution of the energy density with $s_0 = 0.1$. First, r_{in} is evaluated by solving (60) which gives rise to two positive real roots, namely $r_{in} = 4.7424$ and $r_{in} = 8.1051$. Substituting r_{in} in (59) and solving (58) numerically with $C_2(r_{in})$ produces the solution of the energy density function (57). A closed torus structure possessing a cusp, a center, and an outer edge only exists for $r_{in} = 4.7424$, whereas with $r_{in} = 8.1051$, no torus structure could be found. Similarly, for $s_0 = -0.1$ we choose r_{in} that generates a torus configuration.

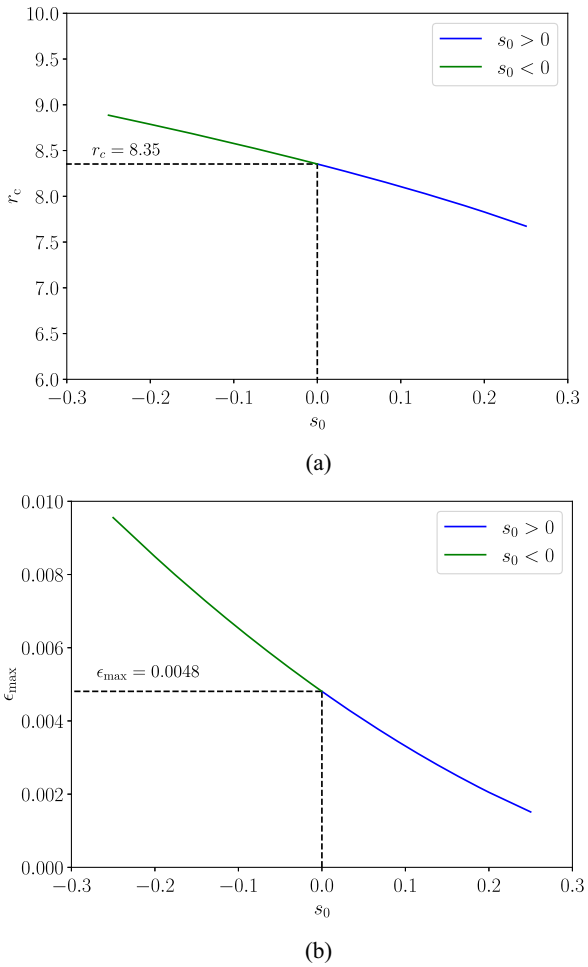

FIG. 2. Behavior of r_c and ϵ_{max} with changing s_0 at the equatorial plane. The black dotted lines in the upper and lower panels denote respective values of ϵ_{max} and r_c for an ideal fluid torus without spin contributions.

The impacts of spin and its coupling to the spacetime curvature of the BH geometry on equilibrium solutions can be appreciated from both the isoenergy density and isopressure contours, as shown, respectively, in Figs. 1(a) and 1(b). Clearly, the radial location of the newly formed center of torus in the presence of spin never coincides with the torus center filled with ideal fluid without spin contributions. Both Figs. 1(a) and 1(b) show this feature where the center r_c of the spin fluid torus gets slightly shifted in comparison to a purely ideal fluid torus. This can be observed for both $s_0 > 0$ and $s_0 < 0$. When compared to the torus without spin fluid ($s_0 = 0$), in the former case, the location of r_c moves toward the horizon and the corresponding magnitude of the maximum energy density well as pressure at r_c gets lowered, whereas in the latter case, r_c moves away from the horizon. The maximum energy density as well as the maximum pressure at r_c get further enhanced for $s_0 < 0$ in comparison to the torus characterized by $s_0 = 0$. Additionally, the size of the torus also gets diminished in the $s_0 > 0$ parameter region. On the other hand, it increases for all values with $s_0 < 0$ and can be clearly noticed from the changes in positions of $r_{\rm in}$ and $r_{\rm out}$ when compared to the equilibrium torus without the Weyssenhoff ideal fluid.

The effect of changing s_0 on the radial position of the center r_c and the corresponding energy density (denoted by $\epsilon_{\rm max}$) can be noticed from Figs. 2(a) and 2(b), respectively. When compared with a purely ideal fluid torus ($s_0 = 0$),

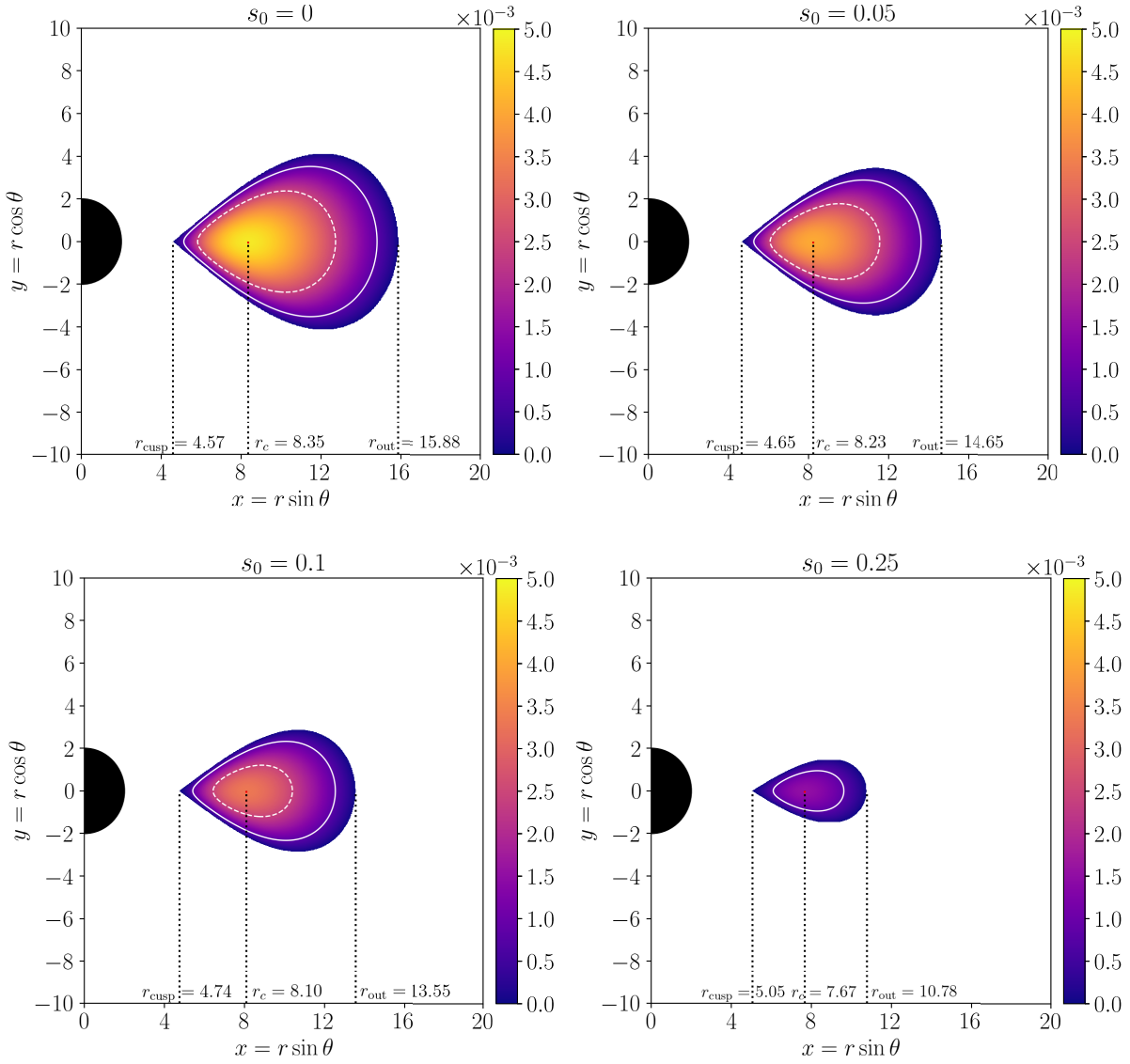

FIG. 3. Isodensity surfaces of a closed torus with $l_0 = 3.8$ and $s_0 > 0$. The small red dot depicts the center of the torus. To furnish a comparison with the $s_0 = 0$ case, same constant density surfaces (solid white and dotted white lines) are shown in all the panels. With the increasing magnitude of s_0, the closed isodensity surfaces become smaller leading to an overall decrease in the size of the torus in comparison to a torus without a spin fluid.

both r_c and $\epsilon_{\max}$ monotonically decrease as s_0 is increased from $s_0 = 0$, whereas if the alignment of the spin is reversed about the equatorial plane, i.e., in the $s_0 < 0$ region, the radial positions of r_c and $\epsilon_{\max}$ increase monotonically. In essence, r_c moves away from the horizon for all $s_0 < 0$ values, resulting in an enhancement of $\epsilon_{\max}$. On the other hand, r_c comes closer to the BH horizon by increasing s_0 with positive values leading to a lowering of $\epsilon_{\max}$ in comparison to a torus without the spin fluid.

The implications of spin-curvature contributions on the morphology of a stationary geometrically thick spin fluid torus are illustrated by the isoenergy density surfaces as shown in Fig. 3 for $s_0 > 0$ and Fig. 4 for $s_0 < 0$. In Fig. 3, one finds that increasing s_0 leads to significant changes on the morphology of the torus. First, the radial position of r_{cusp} shifts further away in comparison to r_{cusp} of the torus with $s = 0$. At the same time, with a further increase in s_0, r_{out} slowly moves closer to r_{cusp} resulting in a decrease in the overall size of the torus, which can be particularly noted for $s_0 = 0.25$. On the other hand, due to the spin and its coupling to curvature, the energy density at the center of the torus diminishes and the corresponding radial position slowly gets closer to the BH horizon. Such a feature is also observed in Fig. 2(a) where the analysis is carried out at the equatorial plane. Second, the overall energy density of the torus gets systematically reduced with an increasing magnitude of s_0. Third, the spin fluid contributes to the redistribution of the isodensity surfaces which can be observed from Figs. 3 and 4, respectively. For the purpose of illustration, it is observed that the reference contour lines

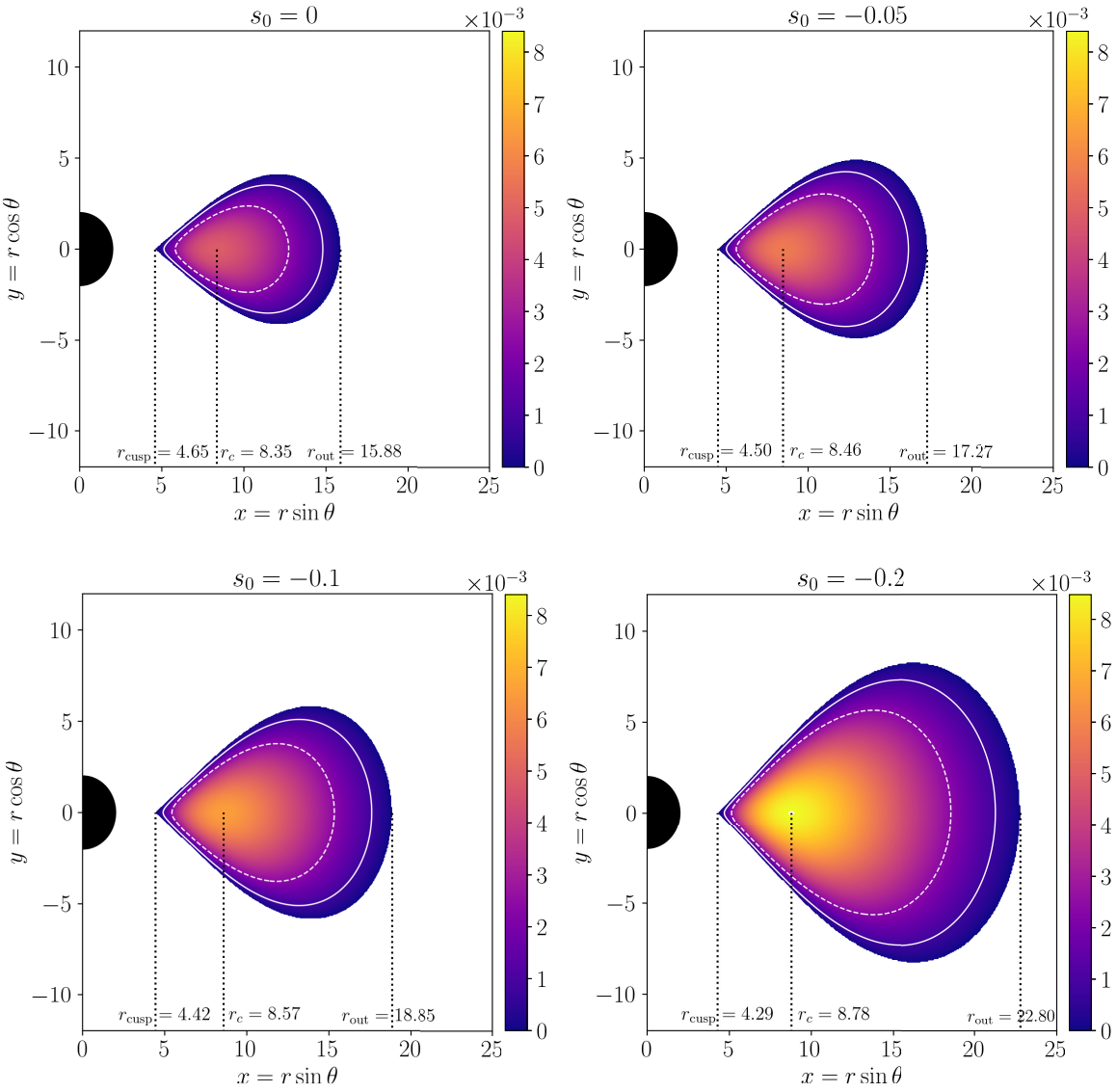

FIG. 4. Isodensity surfaces of the closed torus for $s_0 < 0$ and $l_0 = 3.8$. The small red dot depicts the center of the torus. To furnish a comparison with an ideal fluid torus, the same constant density surfaces (solid white and dotted white lines) are shown in all three panels which spread away, leading to an increase in the size of the torus.

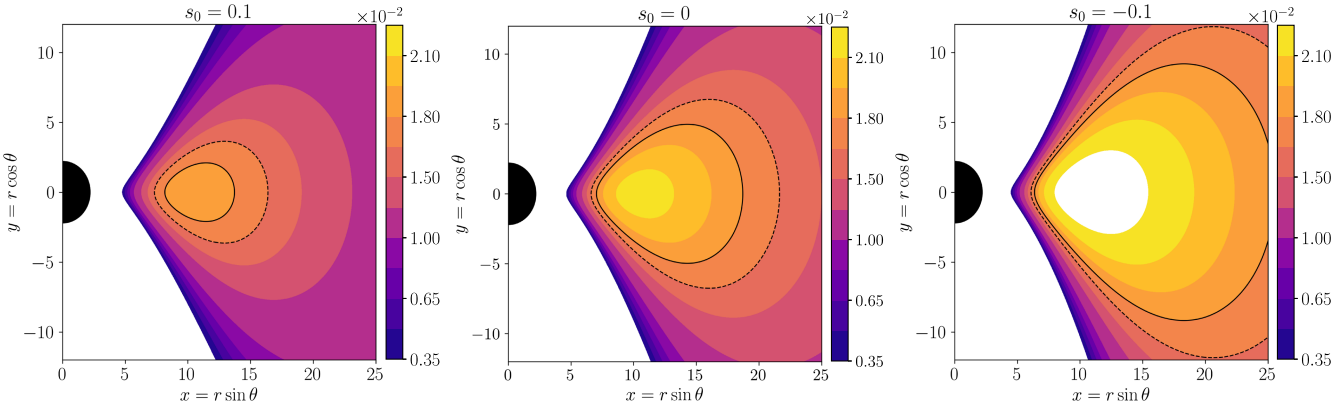

FIG. 5. Isodensity surfaces of an equilibrium torus corresponding to $s_0 < 0, s = 0, s > 0$ with $l_0 = 4$. These tori are characterized by a cusp, a center but are closed at infinity. The black solid and the black dotted lines illustrate redistribution of the same isodensity surfaces for three different values of s_0.

$\epsilon_{\max,0}/3$ (dashed white line) and $\epsilon_{\max,0}/4$ (white line) ($\epsilon_{\max,0}$ is the maximum energy density for $s_0 = 0$) shrink and become smaller with increasing s_0.

However, the scenario is exactly reverse in the $s_0 < 0$ region as shown in Fig. 4. Due to the opposite alignment of spin (at the equatorial plane) the overall size of the torus gets enlarged resulting in a larger difference between r_{cusp} and r_{out}, which can be particularly observed for $s_0 = -0.2$ in Fig. 4. In this case, the energy density at r_c also increases while the location of r_c shifts away from the horizon of the BH. Notably, as s_0 is reduced further, the overall energy density of the torus gets enhanced. Similar to $s_0 > 0$ torus configurations, the redistribution of constant density surfaces can be observed where the contour lines expand, increasing in the overall size of the torus.

By following a similar procedure as discussed before, the isodensity surfaces for $l_0 = 4$ are illustrated in Fig. 5 demonstrating a comparison between $s = 0$ and $s_0 \neq 0$ tori. These constant density surfaces possess a cusp and a center but are closed at infinity, a feature also found in equilibrium solutions without a spin fluid in the Schwarzschild spacetime [31]. Note that in the presence of spin, the fluid lines move outwards for $s_0 < 0$ and inwards for $s_0 > 0$ in comparison to $s = 0$. To highlight the spin-curvature effects and facilitate the comparison with the no-spin fluid torus configuration, we have plotted the same isodensity surfaces, namely $\epsilon = 0.0165$ (dotted black line) and $\epsilon = 0.018$ (solid line) for all three cases. Similar to the case of $l_0 = 3.8$, the effects of spin can be observed from the movement of constant density surfaces which for $s_0 > 0$ come closer, whereas they move away for $s_0 < 0$ when compared with the ideal fluid torus.

Figure 6 presents the profiles of the spin length function at the equatorial plane for different values of l_0 and $s_0 > 0$. The figure shows that by increasing l_0, the peak value of $S(r)$ at the equatorial plane denoted by $S_{\max}$ increases further, the highest being for $l_0 = 4$, for which the torus is closed at infinity. The corresponding radial position denoted by $r_{\max}$ is found to be steadily shifting away from the BH horizon. Furthermore, r_{out} also increases with l_0, implying an increase in size of the torus, which can be observed from the point of intersection of $S(r)$ with the x axis. In Table I, the solutions of $S_{\max}$ and $r_{\max}$ for a representative value of $s_0 = 0.001$ are presented, from which it is readily observed that $r_{\max}$ never coincides with r_c. On the other hand, for $s_0 < 0$ the spin length function takes negative values due to the negative sign of s_0. Once again, similar to the $s_0 > 0$ case, $r_{\max}$ does not coincide with r_c while $S_{\max}$ and r_{out} decrease with l_0. In Table II, representative values of l_0 (which generates solutions of equilibrium tori) are chosen to illustrate the behavior of $S_{\max}$ and $r_{\max}$ due to changing values of s_0. For a fixed l_0, $S_{\max}$ increases but $r_{\max}$ decreases in the $s_0 > 0$

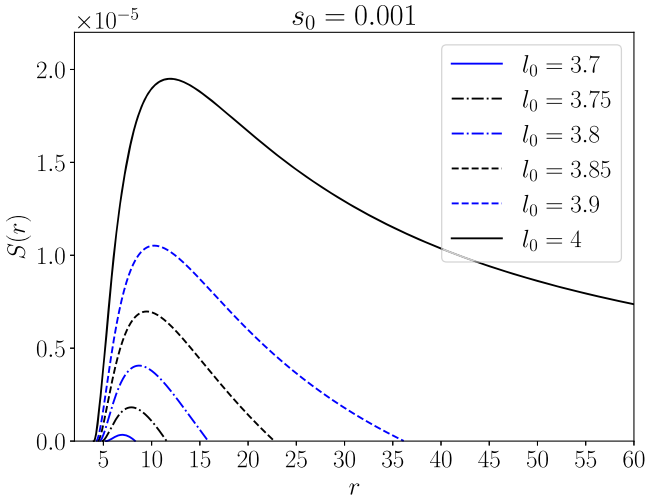

FIG. 6. Profiles of $S(r)$ at the equatorial plane for different values of l_0 and a fixed $s_0 = 0.001$.

TABLE I. Variation of $S_{\max}$ and $r_{\max}$ for different values of l_0 and fixed s_0.

$s_0 = 0.001$			
l_0	r_c	$S_{\max}$	$r_{\max}$
3.7	6.91	3.73×10^{-7}	6.96
3.75	7.71	1.81×10^{-6}	7.87
3.8	8.35	4.06×10^{-6}	8.69
3.85	8.91	6.97×10^{-6}	6.97
3.9	9.45	1.05×10^{-5}	10.25
4	10.47	1.95×10^{-5}	11.99

region. This picture is opposite for all $s_0 < 0$ cases, where one finds that $S_{\max}$ takes a dip and $r_{\max}$ increases in the similar way as r_c. Table III shows a series of equilibrium models of closed spin fluid torus for both positive and negative values of s_0.

Since the Schwarzschild BH spacetime and the Weyssenhoff ideal spin fluid share the same symmetries, in congruence to the orientation of the spin vector at the equatorial plane, the nonzero contributions of the spin-curvature coupling term only come from $R_{trtr}S^{tr}u^t$ and $R_{r\phi\phi r}S^{r\phi}u^{\phi}$. Together with (20), (21), and (57) we obtain

$$\begin{aligned} R_{trtr}S^{tr}u^t &= \frac{2l_0s_0}{r^4\sin\theta}k(r,\theta)\epsilon(r,\theta) \\ &= \frac{2l_0s_0k}{r^4}\left[\frac{2^{1/4}\kappa C_1(r)(r^3\sin^2\theta - l_0^2(r-2))^{1/4} - \sqrt{\sin\theta}}{\kappa\sin^{3/2}\theta}\right] \end{aligned} \tag{61}$$

and

$$\begin{aligned} R_{r\phi\phi r}S^{r\phi}u^{\phi} &= \frac{l_0s_0k(r,\theta)}{r^4\sin\theta}\epsilon(r,\theta) \\ &= \frac{l_0s_0k}{r^4}\left[\frac{2^{1/4}\kappa C_1(r)(r^3\sin^2\theta - l_0^2(r-2))^{1/4} - \sqrt{\sin\theta}}{\kappa\sin^{3/2}\theta}\right], \end{aligned} \tag{62}$$

TABLE II. The stationary solutions of an ideal Weyssenhoff fluid torus showing the behavior of $S_{\max}$ and $r_{\max}$ with s_0 for both $s_0 > 0$ and $s_0 < 0$. Note that $r_{\max}$ never coincides with the center of the torus r_c.

$l_0 = 3.8,\ \kappa = 1$							
s_0	r_c	$S_{\max}$	$r_{\max}$	s_0	r_c	$S_{\max}$	$r_{\max}$
0.001	8.35	4.06×10^{-6}	8.70	−0.001	8.35	-4.09×10^{-6}	8.71
0.01	8.32	3.93×10^{-5}	8.67	−0.01	8.37	-4.21×10^{-5}	8.73
0.1	8.10	2.78×10^{-4}	8.36	−0.1	8.57	-5.55×10^{-4}	9.03
0.25	7.67	3.11×10^{-4}	7.81	−0.25	8.88	-2.06×10^{-3}	9.51
0.35	7.31	1.17×10^{-4}	7.38	−0.35	9.07	-3.62×10^{-3}	9.82
0.4	7.07	1×10^{-4}	7.12	−0.4	9.16	-4.58×10^{-3}	9.98

TABLE III. Solutions of a stationary equilibrium model closed torus supported by the ideal Weyssenhoff spin fluid for $s_0 \neq 0$. The solutions are compared with the purely ideal fluid torus characterized by $s_0 = 0$.

$S(r,\theta) = s_0k(r,\theta)(1-\Omega l_0)\epsilon(r,\theta),\ l_0 = 3.8, \kappa = 1$											
s_0	r_{cusp}	r_c	$\epsilon_{\max}$	$p_{\max}$	r_{out}	s_0	r_{cusp}	r_c	$\epsilon_{\max}$	$p_{\max}$	r_{out}
0	4.57	8.35	0.0048	2.31×10^{-5}	15.89	0	4.57	8.35	0.0048	2.31×10^{-5}	15.89
0.01	4.59	8.32	0.0046	2.16×10^{-5}	15.63	−0.01	4.56	8.37	0.0049	2.47×10^{-5}	16.15
0.05	4.65	8.23	0.0040	1.62×10^{-5}	15.45	−0.05	4.50	8.46	0.0056	3.18×10^{-5}	17.27
0.15	4.83	7.97	0.0026	7.04×10^{-6}	12.54	−0.15	4.36	8.68	0.0074	5.55×10^{-5}	20.67
0.25	5.05	7.67	0.0015	2.29×10^{-6}	10.75	−0.25	4.23	8.88	0.0095	9.12×10^{-5}	25.33
0.35	5.33	7.31	0.00063	4.04×10^{-7}	9.14	−0.35	4.12	9.07	0.0118	1.40×10^{-4}	32.21
0.45	5.78	6.76	7.52×10^{-5}	5.65×10^{-9}	7.41	−0.45	4.02	9.25	0.0144	2.07×10^{-4}	43.50

where $k(r,\theta)$ is given by (54) and the constant of integration $C_1(r)$ is determined at the equatorial plane. It is observed that the nonzero components of the spin-curvature coupling term given by (61) and (62) are symmetric in both upper and lower hemispheres under our present considerations which therefore indicate a symmetric contribution of spin in both the hemispheres of the torus. Both Figs. 3 and 4 confirm this fact about the stationary equilibrium solutions of the torus obtained with $s_0 \neq 0$ in the presence of spin.

The stationary solutions of the equilibrium torus with the ideal Weyssenhoff spin fluid demonstrate the relocation of radial positions of the cusp and center with changing magnitudes of s_0. The two radial positions correspond to crossing of the actual specific angular momentum and the Keplerian specific angular momentum which are determined from the condition $\frac{\partial_\mu p}{\epsilon+p} = 0 = a_\mu$. In the presence of spin, it is expected the Keplerian specific angular momentum will be modified as well [71] and is determined from the corresponding crossing condition. By putting $\partial_r \epsilon = 0$ in (51) together with (57), the Keplerian specific angular momentum for the spin fluid is then obtained by solving the following equation[2]:

$$[r^3 - l_0^2(r-2)]^{1/4} + \frac{2^{3/4} l_0 s_0 (r-3)[r^3 - l_0^2(r-2)^2]}{C_2(r) r^4 (r-2)(r^3 - l_0^2(r-2))} = 0. \tag{63}$$

One can easily observe that in the absence of spin, the above relation gives rise to $l_0 = l_k$. For a given s_0, Keplerian specific angular momentum is determined by solving (63) for l_0 after substituting $C_2(r)$ from (58).

IV. ESTIMATION OF THE SPIN PARAMETER

The spin function $S(r,\theta)$ plays a crucial role in determining the effects of spin on the equilibrium solutions of a torus. Therefore in order to pinpoint the spin effects for astrophysical objects, it is important to estimate the relevant magnitude of spin.

In geometrized units, length, time, and mass have the same dimensions. In these units, the dimension of the spin tensor is given by $S^{\alpha\beta} = [L]$ using (23) whose nonzero components of spin tensor are given by Eqs. (20) and (21). The dimension of the spin length function is given by $[S] = [L]$. Note that ϵ and k are dimensionless in geometrized units, and from the relation $S = s_0 \epsilon k(1 - \Omega l_0)$, one readily finds the dimension of s_0 as $[s_0] = [L]$.

In order to have a rough estimation of s_0, let us assume that the torus is composed of electrons only. The specific spin (spin per unit mass) $\bar{S}$ of an electron is $(\hbar/2)/m_e = 1.93 \times 10^{-11}$ cm, where m_e is the mass of an electron [72]. In terms of units of mass of a central compact object with $M = 3M_\odot = 4.43 \times 10^5$ cm, the specific spin is given by $\bar{S} = 0.44 \times 10^{-16} m_e M$. On the other hand, we can express the specific spin as $\bar{S} = s_0 k(r,\theta)$. On comparing, $s_0 = 0.44 \times 10^{-16} m_e M$, where the value of $k(r,\theta) = 1$ is taken at the equatorial plane. The electron density within an accretion disk $n = 10^{18}$–10^{23} cm^3. With this, $s_0 \approx 10^2$–10^5 [73]. On the other hand, if the central compact object is a supermassive BH with mass $M = 10^8 M_\odot$, $s_0 = 10^{-6} - 0.1 m_e M \text{cm}^{-3}$.

V. SUMMARY AND OUTLOOK

The study of non-self-gravitating ideal fluid moving in a circular motion under hydrostatic equilibrium in a BH spacetime has remained a topic of active research over a long time, thanks to the simple theoretical framework that can be used for developing analytical stationary equilibrium solutions, which serve as initial data for developing numerical simulations of realistic accretion flows. In this work, we have considered a different matter model where the fluid constituents carry an additional intrinsic angular momentum, proportional to their volume. In this case, the spin angular momentum density of the fluid is described by the rank-two spin tensor which is related to the macroscopic spin vector [see (6)] and the matter model of the torus is described by the neutral ideal Weyssenhoff spin fluid. Subjected to Frenkel SSC, the corresponding momentum balance equation is characterized by its spin and their coupling to curvature of the Schwarzschild BH, all of which have substantial effects on stationary solutions of the equilibrium torus.

By further allowing the spin fluid to undergo circular motion in a stationary and axisymmetric background and taking the orientation of the macroscopic spin vector only perpendicular to the equatorial plane, the present work addresses the following issues. First, we have determined the integrability conditions of the general relativistic momentum conservation equation using the Frenkel SSC. These new sets of integrability conditions are found to be straightforward extensions of Von-Zeipel conditions with additional conditions that emerge solely due to the spin, spacetime curvature of a compact object, and their couplings. Although integrability conditions of spinning *particles* have been earlier addressed (see, for example, [74]), to the best of our knowledge, the integrability conditions of a spin *fluid* moving in stationary and axisymmetric spacetime, are, for the first time, reported in the present work. Second, the existence of integrability conditions has allowed us to determine the spin length function (related to the spin tensor) and hence the complete structure of the spin tensor. Third, using the spin tensor, the general relativistic momentum conservation equation is solved for constructing stationary models of equilibrium tori in Schwarzschild geometry by assuming constant

[2]We thank M. Abramowciz for bringing Ref. [71] to our notice and suggesting the computation.

specific angular momentum distributions and a polytropic equation of state.

Set in this simple scenario, this work presents several novel features as described. Our study reveals that the presence of the coupling term of the spin and the curvature tensor of the central BH has some impact on the morphology of the torus, particularly on the constant energy density surfaces, though, qualitatively, the shape of the spin fluid torus remains similar to that of a purely ideal fluid torus for a given value of l_0. The most pronounced signature of spin is found to be for the case of closed torus configurations. Therefore to furnish a quantitative study for determining the effects of spin on stationary solutions of the torus, the spin length is assigned with a constant free parameter s_0 that is allowed to take both positive and negative values characterizing alignment/anti-alignment of the spin vector perpendicular to the equatorial plane. Then, s_0 is varied systematically from $s = 0$ to both higher positive and higher negative values to analyze the consequences of spin.

It is known that the innermost stable circular orbit (ISCO) of a test particle is modified in the presence of the test particle's spin degree of freedom. For the Schwarzschild spacetime, the ISCO of a spinning particle takes two values corresponding to its two spin orientations [75]. Following this, while considering a spin fluid torus, the positive and negative signs of s_0 will therefore generate two ISCOs of the torus. Together with the change in the size of the torus, it will be possible to differentiate the spin fluid torus with $s_0 > 0$ and $s_0 < 0$ for the same value of l_0.

Our analysis reveals that increasing s_0 from $s_0 = 0$ leads to a decrease in the overall energy density and pressure of the torus. The size of the torus also decreases which can be noticed from the shift of $r_{\rm cusp}$ away from the BH horizon and $r_{\rm out}$ toward the horizon. On the other hand, the separation distance between $r_{\rm cusp}$ and $r_{\rm out}$ increase with a systematic increase in s_0 for anti-alignment of the spin, leading to enhancement of both the energy density and the pressure while also expanding its size. In addition, the center of the torus gets shifted, either away from or toward the horizon depending on s_0 in comparison to an ideal spin fluid torus. Eventually, the maximum energy density at the center of the torus decreases (for tori with $s_0 > 0$) or increases (for tori with $s_0 < 0$). It is further noted that the existence of additional intrinsic spin angular momentum leads to the redistribution of isodensity contours in the torus configurations. On studying independently, from the behavior of the spin function at the equatorial plane with respect to changes in l_0 and s_0 it is found that the radial location corresponding to its maximum value is shifted for all $s \neq 0$ and hence never coincides with the torus center. Finally, the value of s_0 is estimated by considering the torus to be composed of spin $1/2$ particles.

The present work is the first step toward studying the stationary solutions of geometrically thick tori in the presence of the ideal Weyssenhoff spin fluid. We adopted several assumptions and presented a simple model; nevertheless, it is found that the presence of an additional intrinsic angular momentum of fluid elements in the form of spin produces a number of new features on the morphology of a torus. Given the integrability conditions in hand, it will be interesting to investigate the possible changes of the morphology of the torus situated in a rotating background, for example, in the astrophysically relevant Kerr BH spacetime. The other realistic case worth exploring is the case of nonconstant specific angular momentum distributions of the torus. Particularly, for realistic accretion flow, when viscous effects are no longer small enough to be neglected, it would be pertinent to consider shear viscous effects within the spin fluid, for example, using a causal prescription [35]. We leave all these issues for future investigations.

ACKNOWLEDGMENTS

We are thankful to Marek Abramowicz and Vladimir Karas for carefully going through the manuscript and providing us with insightful comments. We are thankful to the anonymous referee for providing valuable suggestions and remarks that contributed to the improvement of the manuscript. The work of S. L. is supported by the Deutsche Forschungsgemeinschaft (DFG) with Grant No. 40401154.

[1] J. R. Oppenheimer and H. Snyder, On continued gravitational contraction, Phys. Rev. **56**, 455 (1939).
[2] Roger Penrose, Gravitational collapse and space-time singularities, Phys. Rev. Lett. **14**, 57 (1965).
[3] R. Abuter *et al.* (GRAVITY Collaboration), Detection of the gravitational redshift in the orbit of the star S2 near the Galactic centre massive black hole, Astron. Astrophys. **615**, L15 (2018).
[4] A. M. Ghez, B. L. Klein, M. Morris, and E. E. Becklin, High proper motion stars in the vicinity of Sgr A*: Evidence for a supermassive black hole at the center of our galaxy, Astrophys. J. **509**, 678 (1998).
[5] John Magorrian *et al.*, The demography of massive dark objects in galaxy centers, Astron. J. **115**, 2285 (1998).
[6] Marta Volonteri, Formation of supermassive black holes, Astron. Astrophys. Rev. **18**, 279 (2010).

[7] John Kormendy and Luis C. Ho, Coevolution (Or Not) of supermassive black holes and host galaxies, Annu. Rev. Astron. Astrophys. **51**, 511 (2013).
[8] Heino Falcke, Fulvio Melia, and Eric Agol, Viewing the shadow of the black hole at the Galactic center, Astrophys. J. Lett. **528**, L13 (2000).
[9] Ramesh Narayan and Jeffrey E. McClintock, Observational evidence for black holes, arXiv:1312.6698.
[10] Kazunori Akiyama *et al.* (Event Horizon Telescope Collaboration), First M87 event horizon telescope results. I. The shadow of the supermassive black hole, Astrophys. J. Lett. **875**, L1 (2019).
[11] Kazunori Akiyama *et al.* (Event Horizon Telescope Collaboration), First Sagittarius A* event horizon telescope results. I. The shadow of the supermassive black hole in the center of the Milky Way, Astrophys. J. Lett. **930**, L12 (2022).
[12] B. P. Abbott *et al.* (LIGO Scientific and Virgo Collaborations), Observation of gravitational waves from a binary black hole merger, Phys. Rev. Lett. **116**, 061102 (2016).
[13] B. Louise Webster and Paul Murdin, Cygnus X-1-a spectroscopic binary with a heavy companion?, Nature (London) **235**, 37 (1972).
[14] J. E. McClintock and R. A. Remillard, The black hole binary A0620-00, Astrophys. J. **308**, 110 (1986).
[15] Jorge Casares, Observational evidence for stellar-mass black holes, IAU Symp. **238**, 3 (2007).
[16] J. Casares and P. G. Jonker, Mass measurements of stellar and intermediate mass black-holes, Space Sci. Rev. **183**, 223 (2014).
[17] Jesus M. Corral-Santana, Jorge Casares, Teo Munoz-Darias, Franz E. Bauer, Ignacio G. Martinez-Pais, and David M. Russell, BlackCAT: A catalogue of stellar-mass black holes in x-ray transients, Astron. Astrophys. **587**, A61 (2016).
[18] R. Abbott *et al.* (LIGO Scientific and Virgo Collaborations), GWTC-2: Compact binary coalescences observed by LIGO and Virgo during the first half of the third observing run, Phys. Rev. X **11**, 021053 (2021).
[19] Juhan Frank, Andrew King, and Derek J. Raine, *Accretion Power in Astrophysics: Third Edition* (Cambridge University Press, 2002).
[20] M. J. Rees, E. S. Phinney, M. C. Begelman, and R. D. Blandford, Ion supported tori and the origin of radio jets, Nature (London) **295**, 17 (1982).
[21] Claudio Fanton, Massimo Calvani, Fernando de Felice, and Andrej Cadez, Detecting Accretion disks in active galactic nuclei, Publ. Astron. Soc. Jpn. **49**, 159 (1997).
[22] Alan P. Marscher, Svetlana G. Jorstad, José L. Gómez, Margo F. Aller, Harri Teräsranta, Matthew L. Lister, and Alastair M. Stirling, Observational evidence for the accretion-disk origin for a radio jet in an active galaxy, Nature (London) **417**, 625 (2002).
[23] Luciano Rezzolla, Luca Baiotti, Bruno Giacomazzo, David Link, and Jose A. Font, Accurate evolutions of unequal-mass neutron-star binaries: Properties of the torus and short GRB engines, Classical Quantum Gravity **27**, 114105 (2010).
[24] Lars Bildsten *et al.*, Observations of accreting pulsars, Astrophys. J. Suppl. Ser. **113**, 367 (1997).
[25] Robert Popham and Rashid Sunyaev, Accretion disk boundary layers around neutron stars: X-ray production in low-mass x-ray binaries, Astrophys. J. **547**, 355 (2001).
[26] F. D. Rosenberg, C. J. Eyles, G. K. Skinner, and A. P. Willmore, Observations of a transient x-ray source with a period of 104 S, Nature (London) **256**, 628 (1975).
[27] M. A. Abramowicz and P. C. Fragile, Foundations of black hole accretion disk theory, Living Rev. Relativity **16**, 1 (2013).
[28] L. Rezzolla and O. Zanotti, *Relativistic Hydrodynamics* (Oxford University Press, Oxford, UK, 2013).
[29] L. G. Fishbone and V. Moncrief, Relativistic fluid disks in orbit around Kerr black holes, Astrophys. J. **207**, 962 (1976).
[30] M. Abramowicz, M. Jaroszynski, and M. Sikora, Relativistic, accreting disks, Astron. Astrophys. **63**, 221 (1978).
[31] J. A. Font and F. Daigne, The runaway instability of thick discs around black holes—I. The constant angular momentum case, Mon. Not. R. Astron. Soc. **334**, 383 (2002).
[32] Q. Lei, M. A. Abramowicz, P. C. Fragile, J. Horak, M. Machida, and O. Straub, The Polish doughnuts revisited I. The angular momentum distribution and equipressure surfaces, Astron. Astrophys. **498**, 471 (2009).
[33] H. Kucáková, P. Slaný, and Z. Stuchlík, Toroidal configurations of perfect fluid in the Reissner-Nordström-(anti-)de Sitter spacetimes, J. Cosmol. Astropart. Phys. 01 (2011) 033.
[34] N. I. Shakura and R. A. Sunyaev, Black holes in binary systems. Observational appearance, Astron. Astrophys. **24**, 337 (1973).
[35] S. Lahiri and C. Lämmerzahl, A toy model of viscous relativistic geometrically thick disk in Schwarzschild geometry, arXiv:1909.10381.
[36] J. Kovář, P. Slaný, Z. Stuchlík, V. Karas, C. Cremaschini, and J. C. Miller, Role of electric charge in shaping equilibrium configurations of fluid tori encircling black holes, Phys. Rev. D **84**, 084002 (2011).
[37] J. Kovář, P. Slaný, C. Cremaschini, Z. Stuchlík, V. Karas, and A. Trova, Electrically charged matter in rigid rotation around magnetized black hole, Phys. Rev. D **90**, 044029 (2014).
[38] P. Slaný, J. Kovář, Z. Stuchlík, and V. Karas, Charged tori in spherical gravitational and dipolar magnetic fields, Astrophys. J. Suppl. Ser. **205**, 3 (2013).
[39] S. S. Komissarov, Magnetized tori around Kerr black holes: Analytic solutions with a toroidal magnetic field, Mon. Not. R. Astron. Soc. **368**, 993 (2006).
[40] Sergio Gimeno-Soler and José A. Font, Magnetised Polish doughnuts revisited, Astron. Astrophys. **607**, A68 (2017).
[41] Sayantani Lahiri, Sergio Gimeno-Soler, José A. Font, and Alejandro Mus Mejías, Stationary models of magnetized viscous tori around a Schwarzschild black hole, Phys. Rev. D **103**, 044034 (2021).
[42] Luciano Rezzolla, Olindo Zanotti, and Jose A. Font, Dynamics of thick discs around Schwarzschild-de Sitter black holes, Astron. Astrophys. **412**, 603 (2003).
[43] P. I. Jefremov and V. Perlick, Circular motion in NUT spacetime, Classical Quantum Gravity **33**, 245014 (2016).

[44] Alejandro Cruz-Osorio, Sergio Gimeno-Soler, José A. Font, Mariafelicia De Laurentis, and Sergio Mendoza, Magnetized discs and photon rings around Yukawa-like black holes, Phys. Rev. D **103**, 124009 (2021).
[45] Maciek Wielgus, Debora Lancova, Odele Straub, Wlodek Kluzniak, Ramesh Narayan, David Abarca, Agata Rozanska, Frederic Vincent, Gabriel Torok, and Marek Abramowicz, Observational properties of puffy discs: radiative GRMHD spectra of mildly sub-Eddington accretion, Mon. Not. R. Astron. Soc. **514**, 780 (2022).
[46] Sebastian Bahamonde, Shokoufe Faraji, Eva Hackmann, and Christian Pfeifer, Thick accretion disk configurations in the Born-Infeld teleparallel gravity, Phys. Rev. D **106**, 084046 (2022).
[47] Marie Cassing and Luciano Rezzolla, Equilibrium non-selfgravitating tori around black holes in parameterised spherically symmetric spacetimes, Mon. Not. R. Astron. Soc. **522**, 2415 (2023).
[48] M. A. Abramowicz, A. Curir, A. Schwarzenberg-Czerny, and R. E. Wilson, Self-gravity and the global structure of accretion discs, Mon. Not. R. Astron. Soc. **208**, 279 (1984).
[49] G. Lodato, Self-gravitating accretion discs, Riv. Nuovo Cimento **30**, 293 (2007).
[50] Nikolaos Stergioulas, An improved method for constructing models of self-gravitating tori around black holes, Int. J. Mod. Phys. D **20**, 1251 (2011).
[51] Patryk Mach, Selfgravitation and stability in spherical accretion, Acta Phys. Pol. B **38**, 3935 (2007).
[52] Patryk Mach and Edward Malec, Steady critical accretion onto black holes: Self-gravity and sonic point characteristics, Phys. Rev. D **105**, 104012 (2022).
[53] Christian G. Boehmer and Piotr Bronowski, The homogeneous and isotropic Weyssenhoff fluid, Ukr. J. Phys. **55**, 607 (2010).
[54] Marek Szydlowski and Adam Krawiec, Cosmological model with macroscopic spin fluid, Phys. Rev. D **70**, 043510 (2004).
[55] B. Kuchowicz, Cosmology with spin and torsion. Part II. Spatially homogeneous aligned spin models with the Weyssenhoff fluid, Acta Cosmol. **4**, 67 (1976).
[56] S. D. Brechet, M. P. Hobson, and A. N. Lasenby, Classical big-bounce cosmology: Dynamical analysis of a homogeneous and irrotational Weyssenhoff fluid, Classical Quantum Gravity **25**, 245016 (2008).
[57] F. Halbwachs, Lagrangian formalism for a classical relativistic particle endowed with internal structure, Prog. Theor. Phys. **24**, 291 (1960).
[58] Jan Weyssenhoff and A. Raabe, Relativistic dynamics of spin-fluids and spin-particles, Acta Phys. Pol. **9**, 7 (1947).
[59] Y. N. Obukhov and V. A. Korotkii, The Weyssenhoff fluid in Einstein-Cartan theory, Classical Quantum Gravity **4**, 1633 (1987).
[60] Y. N. Obukhov and O. B. Piskareva, Spinning fluid in general relativity, Classical Quantum Gravity **6**, L15 (1989).
[61] Myron Mathisson, Neue mechanik materieller systemes, Acta Phys. Pol. **6**, 163 (1937).
[62] A. Papapetrou, Spinning test-particles in general relativity. I, Proc. R. Soc. A **209**, 248 (1951).
[63] W. G. Dixon, Dynamics of extended bodies in general relativity. I. Momentum and angular momentum, Proc. R. Soc. A **314**, 499 (1970).
[64] F. A. E. Pirani, On the physical significance of the Riemann tensor, Acta Phys. Pol. **15**, 389 (1956).
[65] J. Frenkel, Die Elektrodynamik des rotierenden Elektrons, Z. Phys. **37**, 243 (1926).
[66] W. M. Tulczyjew, Motion of multipole particles in general relativity theory binaries, Acta Phys. Pol. **18**, 393 (1959).
[67] W. G. Dixon, Dynamics of extended bodies in general relativity. I. Momentum and angular momentum, Proc. R. Soc. A **314**, 499 (1970).
[68] Theodore Duddell Newton and Eugene P. Wigner, Localized states for elementary systems, Rev. Mod. Phys. **21**, 400 (1949).
[69] K Kyrian and O Semerak, Spinning test particles in a Kerr field, Mon. Not. R. Astron. Soc. **382**, 1922 (2007).
[70] L. Rezzolla, O. Zanotti, and J. A. Font, Dynamics of thick discs around Schwarzschild-de Sitter black holes, Astron. Astrophys. **412**, 603 (2003).
[71] M. A. Abramowicz and M. Calvani, Spinning particles orbiting the Kerr black hole, Mon. Not. R. Astron. Soc. **189**, 621 (1979).
[72] O. Semerak, Spinning test particles in a Kerr field. 1. Mon. Not. R. Astron. Soc. **308**, 863 (1999).
[73] J. A. Garcia, C. Mendoza, M. Bautista, T. Kallman, J. Deprince, P. Palmeri, and P. Quinet, High-density plasma effects in accretion disks around black holes, in *American Astronomical Society Meeting Abstracts #235*, American Astronomical Society Meeting Abstracts Vol. 235 (Honolulu, Hawai, 2020), p. 346.04.
[74] Georgios Lukes-Gerakopoulos, Spinning particles moving around black holes: integrability and chaos, in *Proceedings of the 14th Marcel Grossmann Meeting on Recent Developments in Theoretical and Experimental General Relativity, Astrophysics, and Relativistic Field Theories* (2017), Vol. 2, pp. 1960–1965, arXiv:1606.09430.
[75] Paul I. Jefremov, Oleg Yu. Tsupko, and Gennady S. Bisnovatyi-Kogan, Innermost stable circular orbits of spinning test particles in Schwarzschild and Kerr space-times, Phys. Rev. D **91**, 124030 (2015).